buildings

MDPI

Article

A Numerical and Theoretical Investigation of the Flexural Behavior of Steel–Ultra-High-Performance Concrete Composite Slabs

Changshui Li [1], Boyi Zhao [2], Dawei Hao [1], Xiaolong Gao [2,*], Hao Bian [1] and Xuanzheng Zhang [2]

[1] China Construction Seventh Engineering Division, Co., Ltd., Zhengzhou 450004, China; lichangshui@cscec.com (C.L.); haodw@cscec.com (D.H.); bianhao7@cscec.com (H.B.)
[2] College of Civil Engineering, Henan University of Technology, Zhengzhou 450001, China; iszhaoby@stu.haut.edu.cn (B.Z.); 2023930795@stu.haut.edu.cn (X.Z.)
* Correspondence: gxl0709@haut.edu.cn

Abstract: The steel–Ultra-High-Performance concrete (UHPC) composite slab is a new type of structure made of steel and UHPC connected by pegs, and its flexural mechanical properties and related design methods need to be further investigated. Firstly, a detailed numerical model of the steel UHPC composite slab is established and validated based on previous flexural behavior experimental research. Secondly, the flexural failure mechanisms of steel–UHPC composite slabs are clarified through finite element analysis. Under positive bending moments, when the degree of shear connection is lower than 100%, the ultimate load capacity of the composite slabs is determined by the shear capacity of the pegs. On the contrary, there are no significant changes in the load-carrying capacity of all the specimens, but there is a slight increase in stiffness. Under negative bending moments, the load-bearing capacity, stiffness, and crack resistance of the composite slab are improved as the degree of shear connection and reinforcement ratio increase. Finally, the method used to calculate the flexural capacity of steel–UHPC composite plates under positive and negative bending moments with high accuracy is proposed based on the analytical results. This paper provides a theoretical basis for the design of flexural performance of steel–UHPC composite slab.

Keywords: ultra-high-performance concrete (UHPC); steel–UHPC composite slab; flexural behavior; numerical analysis; calculation method

check for updates

Academic Editor: Zhongya Zhang, Minqiang Meng, Xiujiang Shen and Abedulgader Baktheer

Received: 15 December 2024
Revised: 1 January 2025
Accepted: 5 January 2025
Published: 8 January 2025

Citation: Li, C.; Zhao, B.; Hao, D.; Gao, X.; Bian, H.; Zhang, X. A Numerical and Theoretical Investigation of the Flexural Behavior of Steel–Ultra-High-Performance Concrete Composite Slabs. *Buildings* **2025**, *15*, 166. https://doi.org/10.3390/buildings15020166

Copyright: © 2025 by the authors. Licensee MDPI, Basel, Switzerland. This article is an open access article distributed under the terms and conditions of the Creative Commons Attribution (CC BY) license (https://creativecommons.org/licenses/by/4.0/).

1. Introduction

Ultra-High-Performance Concrete (UHPC) is a novel eco-friendly cement-based composite material designed based on the principles of optimal particle packing, a water-to-binder ratio of less than 0.25, and fiber reinforcement. It is characterized by its ultra-high mechanical strength, enhanced toughness, superior durability, and excellent workability [1–4]. The interfacial bond strength between the UHPC matrix and steel fibers is significantly enhanced, allowing the UHPC matrix to maintain high tensile strength even after cracking. This results in the realization of metal-like tensile behavior and strain-hardening characteristics, which significantly improve the toughness and ductility of UHPC materials [5,6]. Compared to normal concrete (NC) and conventional high-performance concrete (HPC), the durability of UHPC, including resistance to chloride ion penetration and carbonation, is significantly enhanced by its high densification, which enables it to fully adapt to the demanding engineering requirements of harsh environments, such as corrosive and marine

conditions [7,8]. Meanwhile, considering its excellent mechanical properties and ease of construction, UHPC is effectively utilized in the repair and strengthening of existing damaged or aging structures with good interfacial connection properties [9,10]. The mechanical performance and service life of the original structures are significantly enhanced [11–13]. More importantly, UHPC can be used in special scenarios such as large-span bridges, ultra-high-rise buildings and large-span heavy-duty industrial plants, etc., to minimize the amount of material under the condition of meeting the structural design requirements due to its high strength [14,15]. Traditional reinforced concrete slabs and steel–normal concrete slabs are relatively heavy. In composite cable-stayed bridges, the thickness of reinforced concrete slabs is typically greater than 250 mm, with their self-weight accounting for more than 70% of the weight of the bridge deck system [16]. Replacing the concrete layer in steel–concrete composite structures with UHPC can significantly improve the mechanical properties of the structure [17,18]. The new structure with thinner thickness and smaller mass can reduce structural deadweight and realize greater economic benefits. Due to the excellent tensile properties of UHPC, steel–UHPC composite slabs can effectively solve the problem of easy cracking in the negative moment zone of steel–concrete combined girder bridges and further improve the use of steel–concrete combined girder bridges in terms of span and range of application [19].

The application of steel–UHPC composite structures to bridge decks was first proposed by Shao et al. in 2012. Based on practical engineering needs, they conducted full-scale model static load tests. The results demonstrated that the novel steel–concrete composite bridge deck effectively reduced stresses in the deck structure and enhanced its stiffness, fundamentally mitigating the risk of fatigue cracking in the deck and extending the fatigue life of steel bridge decks [20]. In recent years, studies on steel–UHPC composite structures have focused on fatigue testing of steel–UHPC composite slabs [21–23], validating the shear behavior of peg connections [24–26], and optimizing the treatment of wet joints [27–29]. The reliability of the pegs is the basis for the perfect synergy between the steel–UHPC composite slabs, while the diameter size of the pegs and the separation spacing will have an impact on the working condition of the composite plates when subjected to bending loads. Hu et al. [30] validated the finite element model for the shear performance of pegs in steel–UHPC composite slabs. They discussed the effects of welded reinforcements, peg diameter, and spacing on the failure modes, shear capacity, and load-slip behavior of the peg connectors. The results indicated that when the peg diameters are 13 mm, 16 mm, and 19 mm, the group peg effect should be considered, and a shear-slip model for the pegs was established. Lu et al. [31] found that appropriately increasing the embedment depth and diameter of pegs can enhance their ultimate tensile capacity. However, it should be noted that changes in the failure mode may result in no increase or even a reduction in the load-carrying capacity. The bonded interface at the wet joint of steel–UHPC composite slabs is a weak point in the cooperative performance, affecting the structural safety. Ren et al. [28] designed seven steel–UHPC composite slabs and conducted four-point bending tests. The test parameters included reinforcement type, lapping details, joint width, and filling materials. The experimental results showed that all specimens experienced shear failure, with critical shear cracks forming within the shear span. Finally, a cohesive-friction hybrid model was developed. Concrete is known for its excellent compressive strength but exhibits relatively low tensile strength, which often results in the presence of cracks during service conditions [32]. Luo et al. [33] studied the flexural cracking behavior of steel–UHPC lightweight bridge deck systems by designing 40 steel–UHPC composite slabs and 8 steel–UHPC composite beams for transverse and longitudinal cracking tests. The results indicated that increasing the reinforcement ratio, reducing the UHPC cover thickness, decreasing the spacing of peg shear connectors, and thickening the UHPC layer effectively

mitigated the initiation and propagation of cracks in the UHPC layer. Building on this, Wang et al. [34] proposed a theoretical formula for calculating the maximum crack width on the bottom surface of the UHPC layer through a series of experimental studies. This research provides theoretical guidance for the development of steel–UHPC composite structures. Zou et al. [35] proposed a hollow steel–UHPC composite bridge deck system without shear connectors, composed of hollow steel tubes and UHPC, to reduce the self-weight of the deck and enhance its crack resistance and durability. The results demonstrated that the embedded steel tubes and external UHPC achieved excellent composite performance. Additionally, a theoretical formula for predicting the flexural capacity of hollow steel–UHPC composite bridge decks was developed. Li et al. [36] proposed a steel–UHPC composite bridge deck system without longitudinal ribs. Compared to the orthotropic steel–UHPC composite bridge deck system, increasing the thickness of the UHPC layer alone was insufficient to effectively compensate for the stiffness reduction caused by the removal of U-shaped ribs. By reducing the longitudinal support spacing of the bridge deck system, steel consumption could be reduced by 28% and weld length by 80%, significantly lowering the risk of fatigue cracking in the deck. Li et al. [37] conducted flexural experiments on steel–UHPC composite slabs with PBL shear connectors. The results indicated that PBL connectors effectively ensured the integrated force transfer between the steel plate and the UHPC slab, providing the composite slab with excellent ductility under negative bending moments. Xiao et al. [38] investigated the influence of the number and type of shear connectors on the flexural performance of full-scale steel–concrete composite slabs. Their findings revealed that steel–UHPC composite slabs exhibited flexural failure, whereas steel–concrete composite slabs experienced punching shear failure. Among the composite slabs, specimens with sufficient perforated bonding rib shear connectors demonstrated the best flexural performance. In addition, machine learning and artificial neural network approaches are used to construct models of the intrinsic relationships of materials and to study the mechanical properties of composite structures [39–43]. Currently, domestic and international research on steel–UHPC composite structures is primarily conducted within the realm of bridge engineering. Much of this research focuses on meeting the design requirements for steel–UHPC lightweight composite bridge deck engineering, leading to a narrow scope that lacks broad representativeness. Studies on the effects of loading conditions, the degree of shear connection of the pegs and the reinforcement rate on the mechanical properties of steel–UHPC composite panels are still insufficient and lack depth.

In this paper, numerical simulation and theoretical analysis are used to investigate the bending force behavior of steel–UHPC composite slabs. Based on the determined UHPC principal model and damage evolution equations, the finite element numerical model of this paper is validated based on the bending performance tests of eight steel–UHPC composite slabs conducted by Gao et al. [44,45]. On this basis, the effects of parameters such as bending moments, shear connection degree, and reinforcement ratio on the flexural performance of composite slabs are investigated using numerical analysis methods. The failure mechanisms of steel–UHPC composite slabs under positive and negative bending moments are further clarified. Finally, based on the numerical analysis results, an out-of-plane load-bearing capacity calculation method for steel–UHPC composite slabs under positive and negative bending moments is established and compared with the experimental results.

2. Establishment of 3D FE Model

2.1. Cell Type and Mesh

In this paper, the finite element simulation of the steel–UHPC composite slab is carried out in ABAQUS 2020/Standard. The steel–UHPC composite slab is composed of UHPC slab, pegs, a steel plate, and steel reinforcement. Among them, the UHPC slab, pegs, and

steel plate are simulated using the solid element C3D8R in ABAQUS. The reinforcement is simulated using truss element T3D2 and connected to the UHPC slab through embedding. The contact relationship between the pegs and the steel plate is the way the pegs are bound to the steel plate, while the contact relationship between the steel reinforcement and the UHPC slab is achieved through the steel reinforcement mesh built into the UHPC. In order to reduce the computational time, a 1/4 finite element model of the steel–UHPC composite slab is built for computational analysis due to its inherent biaxial symmetry. The finite element analysis results are significantly affected by the cell mesh size in the model. In order to ensure an accurate result, the meshing rules of each model in this paper are determined after checking the calculation. The finite element model meshing schematic is shown in Figure 1. The mesh size of the pegs is 4 mm, and the mesh size at the location of the peg holes in the UHPC slab is consistent with the outer surface of the pegs, increasing from 4 to 10 mm with the pegs as the center, in which the mesh size of the UHPC between the two pegs is 10 mm. The grid of the contact surface of the steel plate and the UHPC slab is consistent with the grid of the UHPC, with the grid size ranging from 4 mm to 10 mm, and the thickness of the steel plate is divided into three layers.

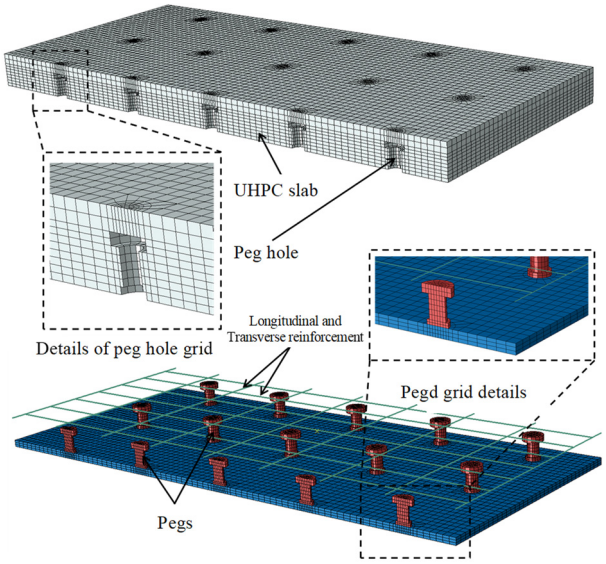


Figure 1. Schemes follow the same formatting.

2.2. Boundary Constraints and Loading Conditions

In order to avoid stress concentration, rigid pads with the same width as the width of the support and loaded beam in the test are set at the loading point and the support location, and the loads are applied to the upper rigid pads in the form of vertical displacements through the reference point. The hard contact mode in the normal direction and the penalty friction with a 0.25 friction coefficient in the tangential direction are used to define the contact relationship between the rigid pads and the composite slab at the bearing position [46,47]. Displacement constraints in three translational directions are imposed on the lower surface of the rigid pad at the support location. The finite element model contains two symmetrical surfaces, and the translational degrees of freedom in the normal direction of the symmetry surfaces and the rotational degrees of freedom in the other two directions are constrained.

The contact behavior of peg–UHPC and slab–UHPC is defined by means of Surface to Surface in ABAQUS. The surfaces of the steel plate and the pegs are defined as master surfaces, and the surface of the UHPC is defined as a slave surface. The normal direction of the contact surface is defined as “hard contact”, the tangential direction is defined by

"penalty function", and the friction coefficient is taken as 0.4 [48]. The final finite element model is shown in Figure 2.

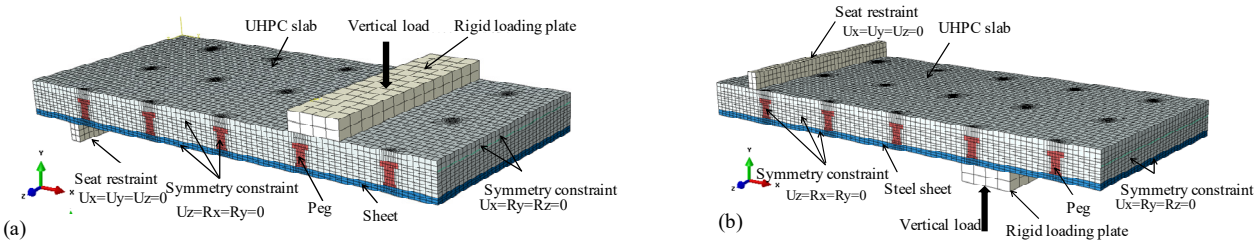


Figure 2. Finite element model of steel–UHPC composite slab: (**a**) Positive bending moment; (**b**) negative bending moments.

2.3. Definition of Material Properties

2.3.1. UHPC

The concrete damage plastic (CDP) model in ABAQUS has good applicability and convergence and is widely used in various applications such as unidirectional loading, cyclic loading and dynamic loading. The CDP model is used to define the constitutive relationships of UHPC in this study, in which the required axial tensile and axial compressive stress–strain relationships and damage variable–inelastic strain relationships are shown in Table 1, and the expressions of the UHPC axial tensile, and axial compressive constitutive relationships (σ_t) are shown in Equation (1) and the expression for the stress–seam width relationship corresponding to the softened section of UHPC is shown in Equation (2). The axial compressive stress–strain curves of UHPC and the corresponding damage variables and the axial tensile stress–seam width curves and the corresponding damage variables are shown in Figures 3 and 4, respectively [49].

Table 1. Mechanical properties of UHPC materials.

Tensile Strength f_{te} (MPa)	Ultimate Tensile Strength f_{tu} (MPa)	Ultimate Tensile Strain ε_{ut} (10^{-6})	Compressive Strength f_{cu} (MPa)	Axial Compressive Strength f_c (MPa)
7.83	9.42	2447	144.1	136

Note: The abbreviation f_{te} refers to the elastic tensile strength, f_{tu} refers to the ultimate tensile strength, ε_{ut} refers to the ultimate tensile strain, f_{cu} refers to the cube compressive strength, f_c refers to axial compressive strength, and the axial compressive strength is 0.95 times the compressive strength [50].

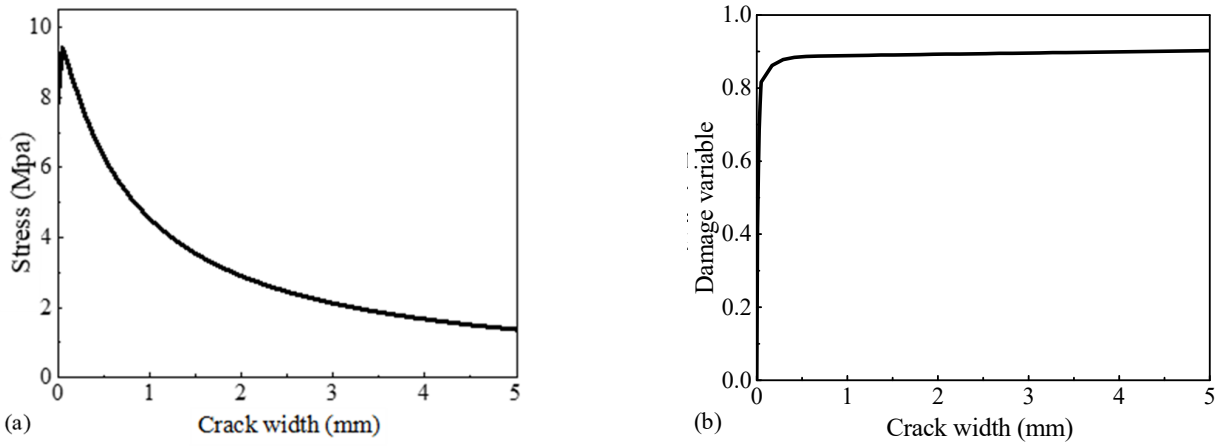


Figure 3. Axial tensile stress–damage relationship of UHPC: (**a**) Axial tensile stress–crack width curve; (**b**) axial tensile damage variables.

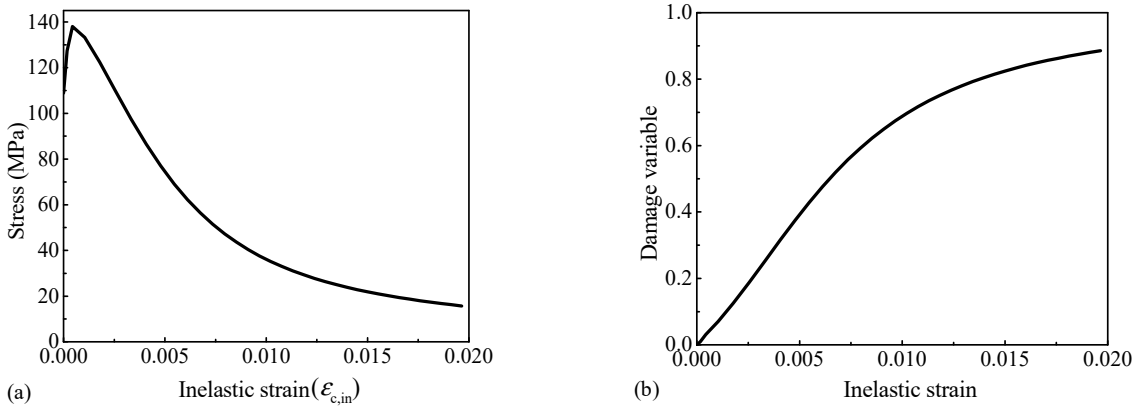


Figure 4. Axial compressive tensile stress–damage relationship of UHPC: (**a**) Axial compressive stress–strain curve; (**b**) axial compressive damage variables.

$$\sigma_t(w) = f_{te} + \frac{f_{tu} - f_{te}}{w_0} w \quad (0 < w < w_0) \tag{1}$$

where w refers to the crack width and w_0 refers to the ultimate tensile strength corresponding to a crack width of 0.05 mm.

$$\sigma_t(w) = f_{tu} \frac{1}{p_1(\frac{w}{w_0} - 1)^{p_2} + \frac{w}{w_0}} \quad (w_0 < w < w_u) \tag{2}$$

where p_1 and p_2 are parameters fitted based on the experimental results, -0.982 and 0.996, respectively.

2.3.2. Constitutive Relationship of the Pegs

The triple-fold model shown in Figure 5a is used to define the stress–strain relationship of the pegs [51–53]. According to the experimental test results, the measured tensile bearing capacity of the pegs under the damage state is 92.5 kN (corresponding to an engineering stress of 460.3 MPa), and the yield strength f_y of the pegs is calculated to be 400 Mpa, while the ultimate strength f_u is 460.3 Mpa, the yield strain ε_y is 0.199%, and the ultimate strain ε_u should be taken as 12% [54]. The basic mechanical properties of the peg are shown in Table 2. It should be noted that the measured ultimate strength of the pegs is the engineering stress, while the stress–strain relationship of the material entered in ABAQUS refers to the real stress–strain relationship curve (Figure 5b). It is necessary to convert the engineering stress–strain curve determined by the above parameters to the real stress–strain curve, and the conversion relationship is shown in Equations (3) and (4).

$$\sigma = \sigma_{nom}(1 + \varepsilon_{nom}) \tag{3}$$

$$\varepsilon = \ln(1 + \varepsilon_{nom}) \tag{4}$$

where σ and σ_{nom} refer to the true and engineering stresses, respectively; ε and ε_{nom} refer to the true and engineering strains, respectively.

Table 2. Material mechanical properties of steel and pegs.

Material Type	f_y (MPa)	f_u (MPa)	E_s (GPa)
Peg	400	430	201
Steel	357	462	201
Steel reinforcement	406 Mpa	539	207

Note: The abbreviation f_y refers to the yield strength, f_u refers to the ultimate strength, and E_s refers to the modulus of elasticity.

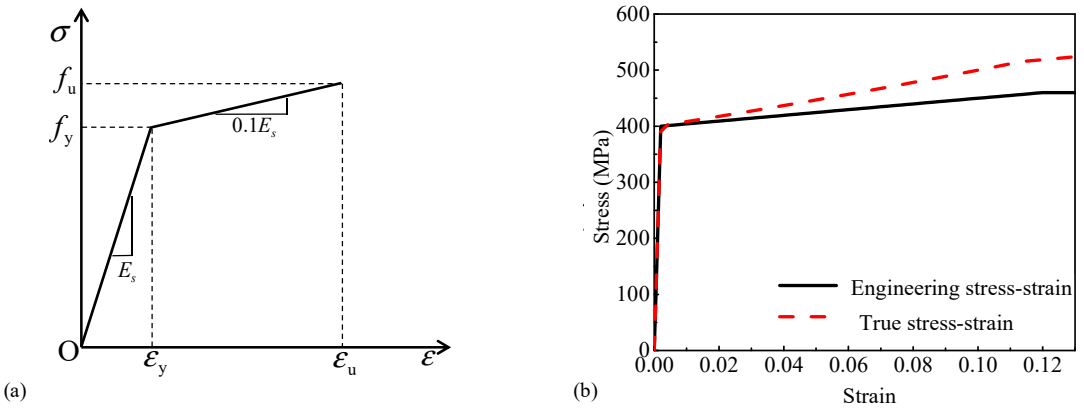


Figure 5. Definition of pegs' stress-strain relationship: (**a**) Trifold model; (**b**) stress-strain curves.

The flexible damage model in the ductile metal damage model is used to describe the damage process of the pegs, and the parameters include equivalent plastic strain, stress triaxiality, and strain rate. According to the Dominic Kruszewski et al. [51], the relationship between equivalent plastic strain and stress triaxiality (ε_{pl}) is shown in Equation (5).

$$\varepsilon_{pl} = \varepsilon_u e^{-\beta(\theta - 1/3)} \tag{5}$$

where ε_u is the ultimate strain; β is the characteristic parameter of the material, which is taken as 1.5; and θ is the stress triaxiality, which ranges from -0.33 to 2.0.

The plastic displacement approach is used to define the damage evolution process of the pegs in this study, where the relationship between the damage variables (D_i) and the plastic displacements (u_i^{pl}) can be determined by calculations based on Equations (6) and (7) [51]. Due to the lack of bolster stress-strain measured data, the definition of the bolster damage evolution process in this paper is determined according to [51], and the corresponding flexible damage model and its damage evolution process are shown in Figure 6.

$$D_i = \alpha_D[1 - \frac{\sigma_i}{f_u}] \tag{6}$$

$$u_i^{pl} = u_f^{pl} \frac{\varepsilon_i^{pl} - \varepsilon_u}{\varepsilon_f^{pl} - \varepsilon_u} \tag{7}$$

where α_D is the correction factor, σ_i is the stress in the descending section, u_f^{pl} is the fracture displacement taken as 1.8 mm, and ε_f^{pl} is the plastic strain at the time of peg fracture.

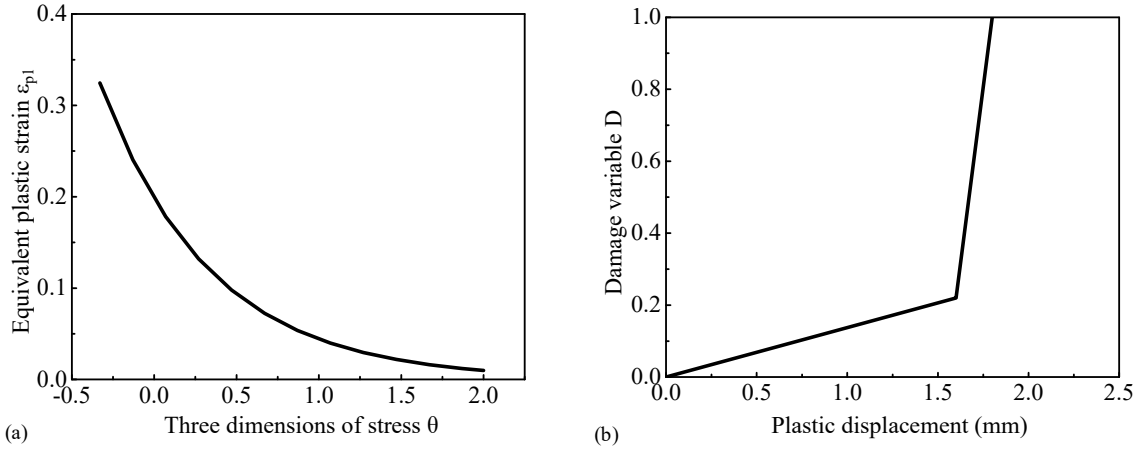


Figure 6. Definition of ductile damage model of pegs: (**a**) Flexible damage model; (**b**) stress-strain curves.

2.3.3. Steel and Steel Reinforcement Constitutive Relation

The isotropic model is used to simulate the steel and steel reinforcement, and the yield criterion adopts the default Mises yield condition in ABAQUS. The stress–strain relationship between the steel plate and reinforcement is defined using a bilinear model as shown in Figure 7, and the basic mechanical properties of the materials are shown in Table 2.

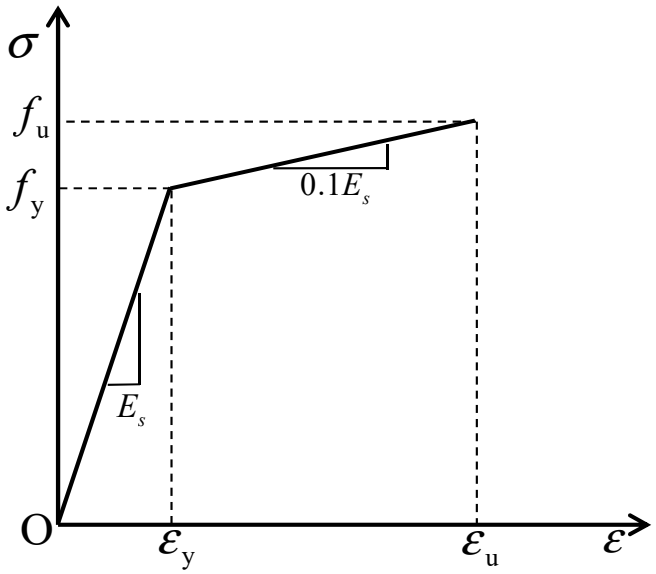


Figure 7. Bilinear model.

3. Validation of the Finite Element Model

In this section, the results of the previous experimental studies are compared with and used to correct the results of the finite element analysis in order to verify the accuracy and validity of the finite element model.

3.1. Experimental Generalization

According to the author's previous research [44], the basic design parameters and constructional diagrams of the tests are shown in Table 3 and Figure 8, respectively, and the test loading device and the main test results are shown in Figure 9 and Table 4.

Table 3. Basic design parameters of steel–UHPC composite slab specimens.

Specimen Number	s_a (mm)	s_b (mm)	s_c (mm)	s_d (mm)	r_a (mm)	r_b (mm)	ρ (%)	Loading Method
P-SUCS-3.1%-150	150	150	125	50	50	100	3.1	P
P-SUCS-3.1%-200	200	200	100	50	50	100	3.1	P
P-SUCS-3.1%-250	250	250	175	100	50	100	3.1	P
N-SUCS-3.1%-150	150	150	125	50	50	100	3.1	N
N-SUCS-3.1%-200	200	200	100	50	50	100	3.1	N
N-SUCS-3.1%-250	250	250	175	100	50	100	3.1	N
N-SUCS-2.0%-200	200	200	100	50	80	100	2.0	N
N-SUCS-3.8%-200	200	200	100	50	40	100	3.8	N

Note: s_a and s_b refer to the longitudinal and transverse spacing of the pegs. S_c and s_d refer to the longitudinal and transverse edge spacing of the pegs. R_a and r_b refer to the spacing of the transverse and longitudinal steel reinforcement. P refers to the steel reinforcement ratio of longitudinal steel reinforcement in UHPC. The specimens are named P and N for positive and negative moment loading, respectively. SUCS is the acronym used for the steel–UHPC composite slab and the numbers at the end represent the spacing of the pegs.

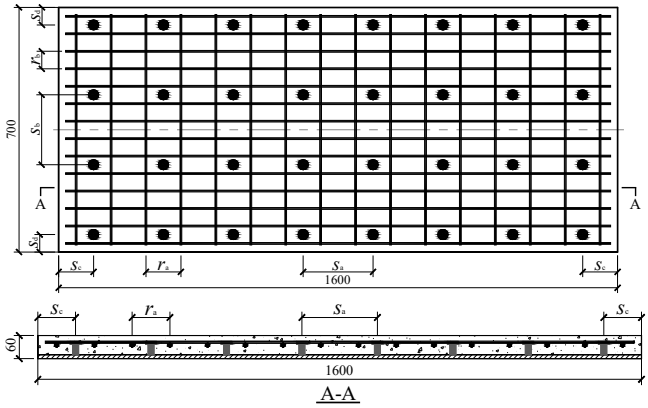


Figure 8. Dimensions of composite slab specimens.

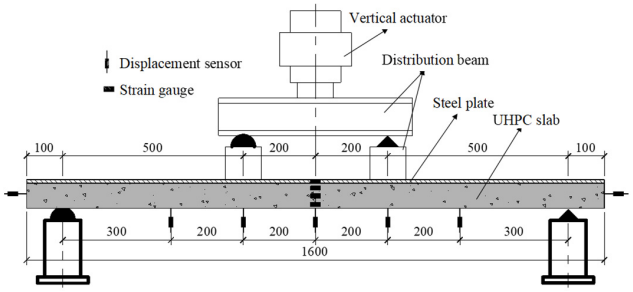


Figure 9. Schematic diagram of loading device.

Table 4. Test results of steel–UHPC composite slab specimens.

Specimen Number	P_{cr} (kN)	δ_{cr} (mm)	P_y (kN)	δ_y (mm)	$P_{u,Test}$ (kN)	δ_u (mm)	$\varepsilon_{y\text{-}s}$ (10^{-6})	$\varepsilon_{u\text{-}s}$ (10^{-6})
P-SUCS-150-3.1%	235.1	15.7	271.7	20.82	320.2	27.94	3097	4606
P-SUCS-200-3.1%	170.1	11.23	261.8	26.37	285.7	34.19	1772	3373
P-SUCS-250-3.1%	94.68	8.42	-	-	174.9	27.58	1542	3915
N-SUCS-3.1%-150	29.3	1.96	113.0	23.60	119.3	42.65	-	-
N-SUCS-3.1%-200	24.4	1.24	100.1	25.49	112.6	64.27	-	-
N-SUCS-3.1%-250	20.1	0.95	99.2	30.91	110.5	62.69	-	-
N-SUCS-2.0%-200	23.6	1.22	81.1	22.84	86.8	48.26	-	-
N-SUCS-3.8%-200	23.4	1.27	114.4	28.66	128.6	57.20	-	-

Note: P_{cr} and δ_{cr} represent the load and deflection when the crack width reaches 0.05 mm, P_y and δ_y represent the load and deflection when the steel plate yields, $P_{u,Test}$ and δ_u represent the ultimate load and deflection of the specimen, and $\varepsilon_{y\text{-}s}$ and $\varepsilon_{u\text{-}s}$ represent the maximum tensile strain of the steel plate and the maximum compressive strain of the UHPC, respectively, at the ultimate load.

3.2. Numerical Analysis of Steel–UHPC Composite Slabs Under Positive Bending Moments

3.2.1. Load–Deflection Curve

Under the action of positive bending moment, the load–deflection curves obtained from numerical analysis of steel–UHPC composite slabs are compared with the test results [44] as shown in Figure 10a–c. As shown in the figures, the load–deflection curves obtained via the numerical analysis can basically match the test results in the rising section. Table 5 lists the finite element calculation results and test results of the ultimate load capacity of the composite slab. The degree of shear connection between spigot and UHPC can be calculated according to the method of calculating the degree of shear connection of steel-mixed composite beams (ψ) [55], and the calculation formula is shown in Equation (8).

$$\psi = nP_{peg}/F_{min} \tag{8}$$

where n is the number of pegs in the shear span section of the steel–UHPC composite slab specimen. P_{peg} is the shear ultimate bearing capacity of the pegs. F_{min} is the smaller value of the tensile or compressive bearing capacity of the steel plate or UHPC.

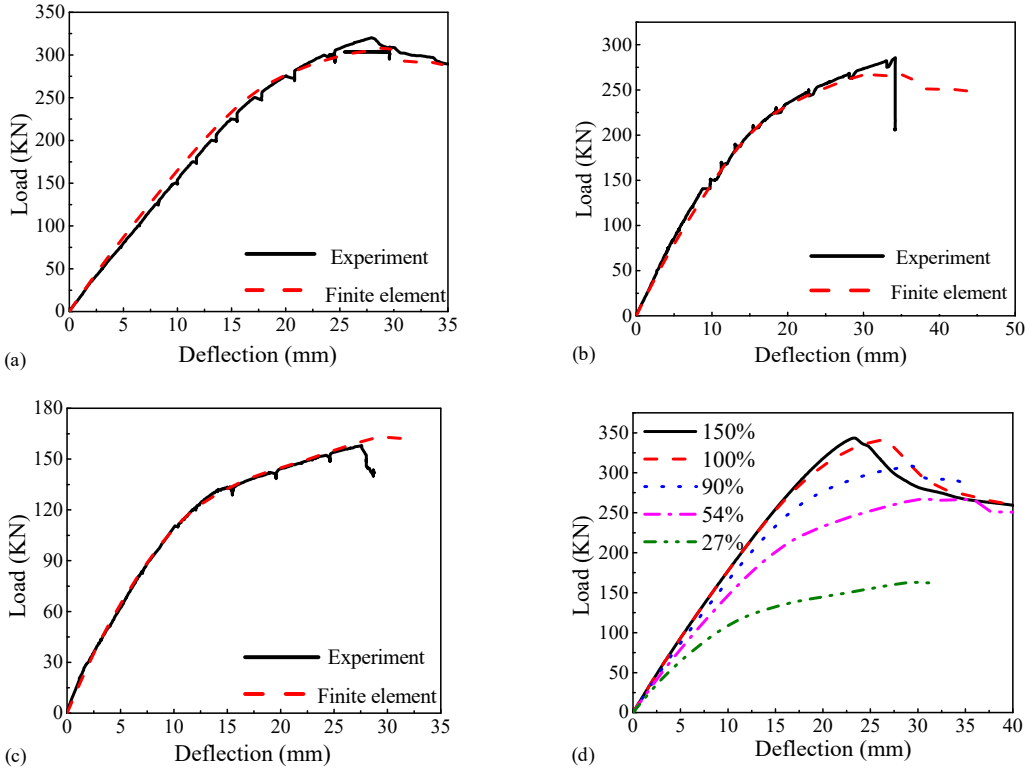


Figure 10. Finite element calculation results of steel–UHPC composite slabs: (**a**) Specimen P-SUCS-3.1%-150; (**b**) specimen P-SUCS-3.1%-200; (**c**) specimen P-SUCS-3.1%-250; (**d**) different shear connection degree.

Table 5. Ultimate bearing capacity of composite slabs under positive bending moments.

Specimen Number	Shear Connection Degree	$P_{u,Test}$ (kN)	$P_{u,FEA}$ (kN)	$P_{u,Test}/P_{u,FEA}$
P-SUCS-3.1%-150	90%	320.2	310.7	1.03
P-SUCS-3.1%-200	54%	285.7	267.1	1.07
P-SUCS-3.1%-250	27%	159.1	162.9	0.96
P-SUCS-3.1%-150-FEA1	100%	-	340.5	-
P-SUCS-3.1%-150-FEA2	150%	-	343.5	-

Note: $P_{u,FEA}$ refers to the ultimate bearing capacity value of the finite element analysis results.

The shear capacity of the peg connections (P_u) in UHPC is determined according to Equation (9), which was established in a previous study [45], and the calculation formula is shown in Equation (9).

$$P_u = A_{sc} f + \eta f_c d_{wc} l_{wc} \quad (9)$$

where A_{sc} refers to the cross-sectional area of the peg, f refers to the design value of the tensile strength of the peg, and d_{wc} and l_{wc} refer to the diameters and heights of the peg weld, respectively. η refers to the correction factor for the size of the weld, which is taken as 1.5 [38], whereas Luo suggested a correction factor of 2.5. After attempting the calculations, 2.0 was selected as the correction factor in this paper and was used to accurately assess the shear capacity of the peg connections [33].

As shown in Table 5, it can be seen that the average ratio between the test results and the finite element calculation results is 1.03, which is indicative of a high accuracy. A comparison of the curves for different degrees of peg connections is given in Figure 10d, where the specimens with 100% and 150% degree of connection are obtained by scaling up the yield and ultimate strengths of the pegs with equal proportions on the basis of P-SUCS-3.1%-150. According to Figure 10d and Table 5, for the specimens obtained after the

degree of shear connection reaches 100%, the final damage state depends on the ultimate strengths of the steel plate and the UHPC. Therefore, the increase in the degree of shear connection will no longer cause a change in the ultimate load capacity of the specimen. Before 80% of the ultimate load capacity is reached, the peg connections of each specimen are in an elastic state and there is no significant difference in the flexural stiffness of each specimen. For specimens with less than 100% shear connection, the ultimate load capacity of the specimen depends on the ultimate shear capacity of the connection. A reduction in the degree of shear connection will result in a significant decrease in both the ultimate load-carrying capacity and the stiffness of the specimen.

3.2.2. Analysis of Damage Mechanism of Specimen

The finite element models of steel–UHPC composite slabs with shear connection degrees of 54% and 100% are subjected to ultimate loads, as depicted in Figures 11 and 12. As shown in Figure 11, the peg root of specimen P-SUCS-3.1%-200, which has a shear connection degree of 54%, exhibits an equivalent plastic strain ranging from 0.09 to 0.18. Significant plastic deformation leads to visible damage in the UHPC at the pegs' root. When the specimen reaches the ultimate load, significant compression damage occurs on the top surface of UHPC, with a thickness range of about 10 mm and a compression damage variable below 0.83, consistent with the failure mode observed in the test. From Figure 12, it can be observed that for the model with a shear connection degree of 100%, the pegs exhibit significant plastic deformation at the ultimate load. However, the equivalent plastic strain at the base of the pegs, ranging from 0.06 to 0.11, is lower than that of the pegs at the base of the composite slab specimen with a shear connection degree of 54%. As shown in Figure 12a, there is a noticeable increase in the compressive damage area on the upper surface of the UHPC board, extending downward to a depth of approximately 17 mm, while fully exerting its compressive strength.

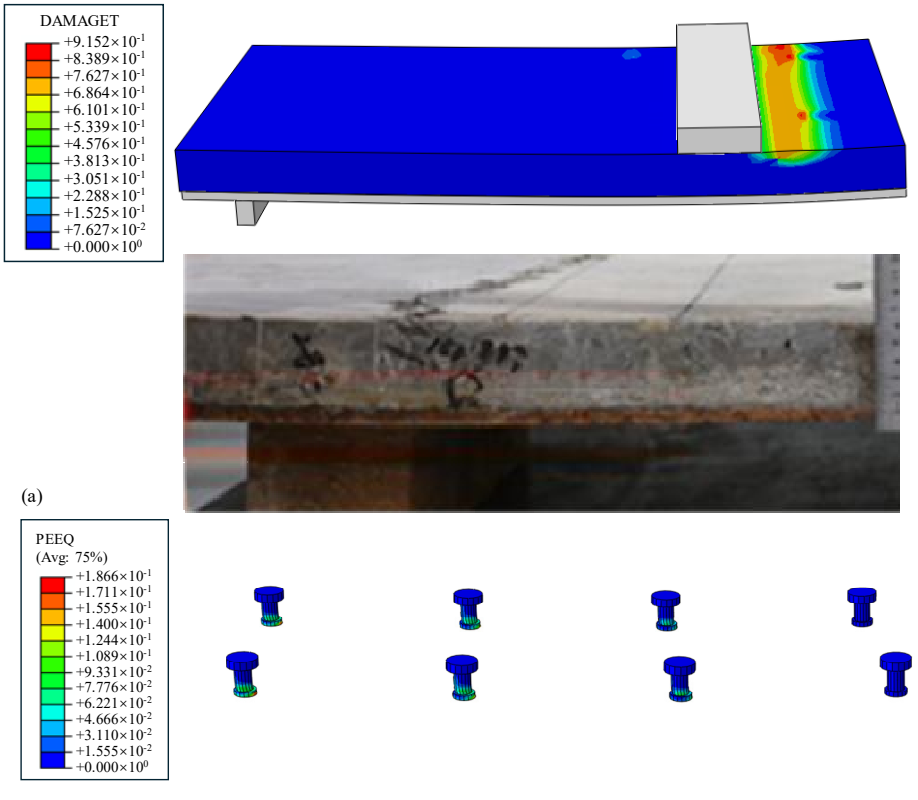
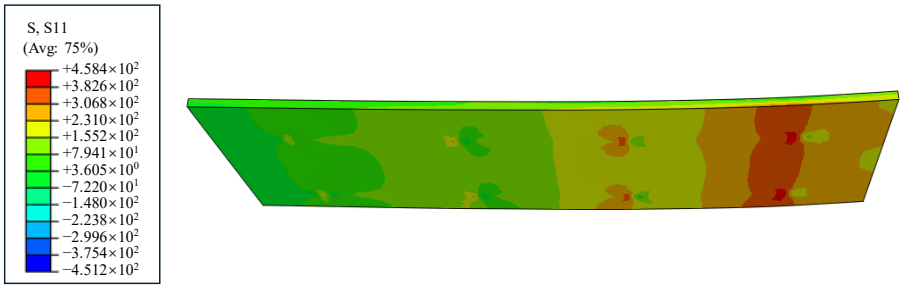
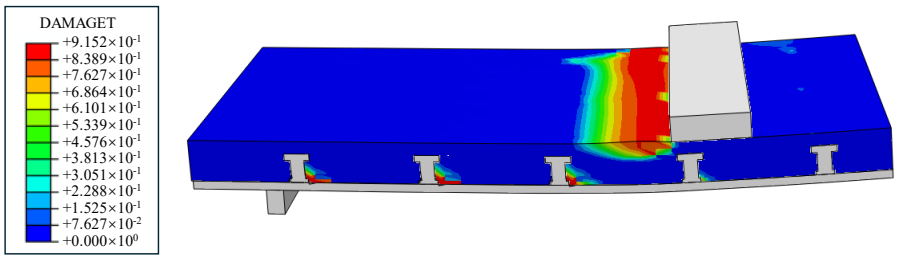


Figure 11. *Cont.*

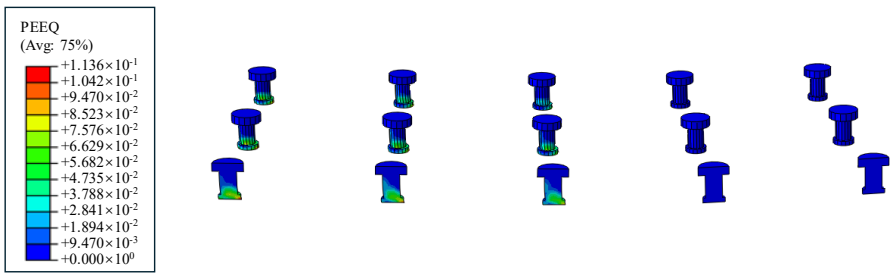


(c)

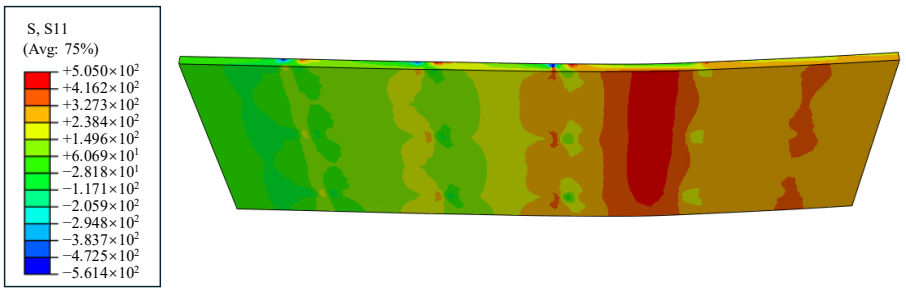
Figure 11. Analysis results of composite slabs with 54% shear connection degree: (**a**) Pressure damage contours for UHPC slab; (**b**) plot of equivalent plastic strain distribution of pegs; (**c**) longitudinal stress contours of steel plate.



(a)



(b)



(c)

Figure 12. Analysis results of composite slab with 100% shear connection degree: (**a**) Pressure damage contours for UHPC slab; (**b**) plot of equivalent plastic strain distribution of pegs; (**c**) longitudinal stress contours in a steel plate.

The longitudinal stress distributions of steel plates with varying degrees of shear connection are presented in Figures 11c and 12c. In comparison, when the specimen reaches the ultimate load, the composite slab with a shear connection degree of 54% exhibits tensile stress on the lower surface of the steel plate in the pure bending region, with a corresponding tensile stress of 386.96 MPa. Meanwhile, the upper surface is in a compressed state, with a corresponding compressive stress of −85.93 Mpa. For the composite slab with a shear connection degree of 100%, the entire cross-section of the steel plate in the pure bending region is under tension. The tensile stresses corresponding to the lower and upper surfaces of the steel plate are 471.4 Mpa and 68.1 Mpa, respectively.

In summary, under the action of positive bending moment, insufficient shear connection of the pegs hinders the complete transfer of shear forces between the steel plate and the UHPC slab, as it is limited by the shear capacity of the connectors. This compromises the collaborative performance of the steel plate and UHPC slab, preventing the full utilization of their material properties.

3.3. Numerical Analysis of Steel–UHPC Composite Slabs Under Negative Bending Moments

3.3.1. Load–Deflection Curves

Under the action of a negative bending moment, the load–deflection curves obtained through finite element calculations are compared with the test results, as shown in Figure 13a–e. The comparison reveals that the load–deflection curve from finite element calculations is generally consistent with the test results, and the characteristic points of the curve align well with the test outcomes. Table 6 lists the finite element calculation results and test results for the ultimate load-carrying capacity of the composite slab. It can be observed that the average ratio between the test results and the finite element calculation results is 1.01, indicating high accuracy. The degree of shear connection listed in Table 6 is calculated according to Equation (8). However, under negative bending moments, the steel plate is compressed, while the UHPC slab is undergoing tension. Therefore, F_{min} in Equation (8) should take the smaller value between the compressive capacity of the steel plate and the tensile capacity of the UHPC slab. When calculating the tensile capacity of the UHPC slab, the contribution of the reinforcement to the overall capacity should be considered.

Table 6. Ultimate bearing capacity of composite slabs under negative bending moments.

Specimen Number	Degree of Shear Connection	$P_{u,Test}$ (kN)	$P_{u,FEA}$ (kN)	$P_{u,Test}/P_{u,FEA}$
N-SUCS-3.1%-150	250%	116.3	118.1	0.98
N-SUCS-3.1%-200	200%	112.6	110.9	1.02
N-SUCS-3.1%-250	100%	110.5	108.2	1.02
N-SUCS-2.0%-200	200%	86.8	87.4	0.99
N-SUCS-3.8%-200	200%	128.2	127.1	1.01
N-SUCS-3.1%-250-FEA1	50%	-	102.9	-
N-SUCS-3.1%-250-FEA2	0%	-	79.6	-
N-SUCS-4.5%-200	200%	-	136.2	-
N-SUCS-6.1%-200	200%	-	158.1	-

The comparison results of the load–deflection curves for steel–UHPC composite slabs with different shear connection degrees under negative bending moments are presented in Figure 13f. It can be observed that when the degree of shear connection is 100% or greater, the shear capacity of the connector surpasses the tensile strength of the UHPC layer that incorporates the steel reinforcement. By further increasing the degree of shear connection, the flexural stiffness of the specimen will undergo a significant improvement; bending stiffness increases by 34.73% when the degree of shear connection is increased from 100% to 250%. However, the ultimate bearing capacity of the specimen remains largely unchanged, as it is constrained by the tensile strength of the UHPC and the reinforcement. When the shear connection is insufficient, as indicated in Table 6 and Figure 13f, reducing the degree of shear connection from 100% to 50% leads to a 4.8% decrease in the ultimate load capacity of the specimen. Moreover, the flexural stiffness of the specimen is significantly reduced by 30.45%. The main reason for this is that as the shear connection degree of the composite slab decreases, the restraining effect of the steel plate on the deformation of the UHPC weakens. This leads to faster development of crack widths in the UHPC, resulting in a significant reduction in the stiffness of the specimen.

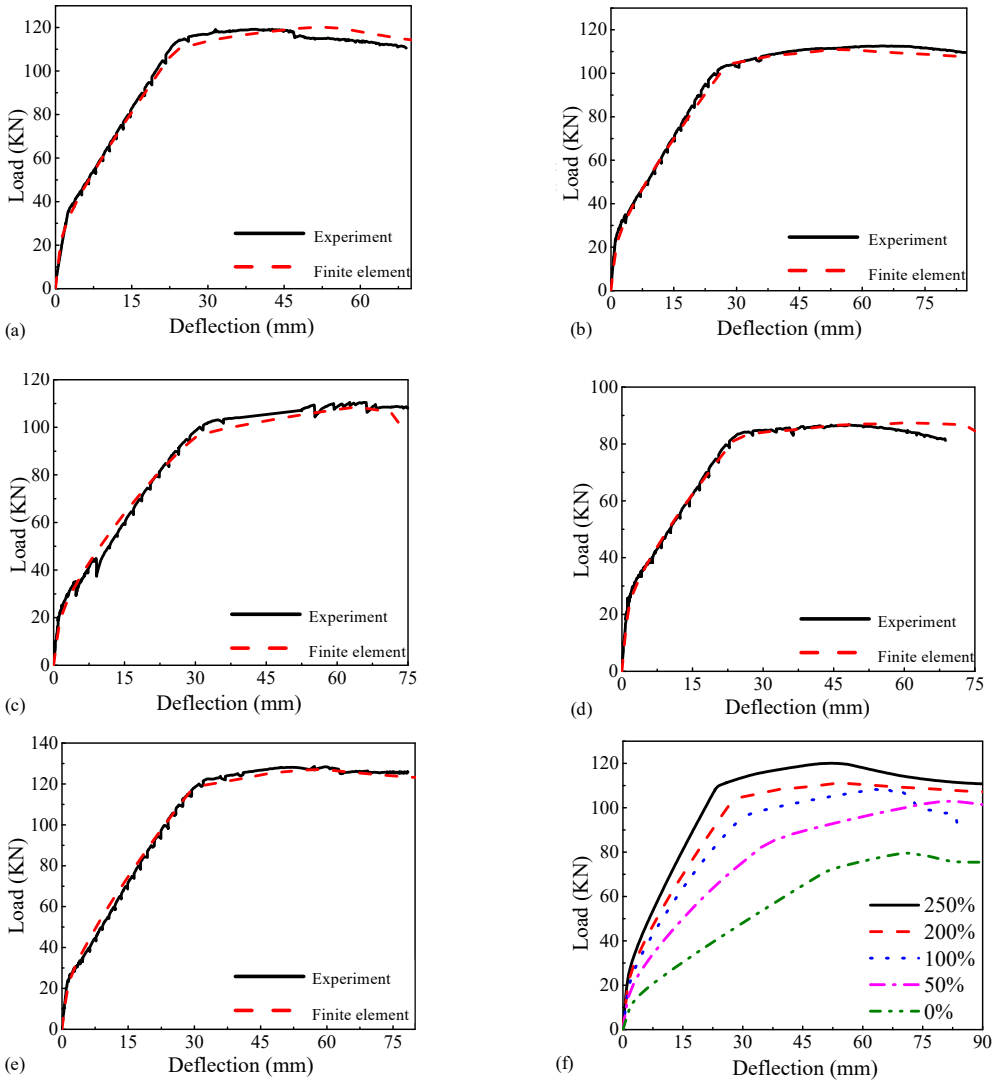


Figure 13. Finite element calculation results of steel–UHPC composite slabs: (**a**) Specimen N-SUCS-3.1%-150; (**b**) Specimen N-SUCS-3.1%-200; (**c**) Specimen N-SUCS-3.1%-250; (**d**) Specimen N-SUCS-2.0%-200; (**e**) Specimen N-SUCS-3.8%-200; (**f**) different shear connection degree.

The load–deflection curves of steel–UHPC composite slabs with different reinforcement ratios, obtained from finite element analysis, are shown in Figure 14. It can be observed that under negative bending moments, both the flexural stiffness and ultimate load capacity of the specimen increase significantly with the reinforcement ratio. This indicates that increasing the reinforcement ratio further enhances the load-bearing capacity and crack control ability of the UHPC slab.

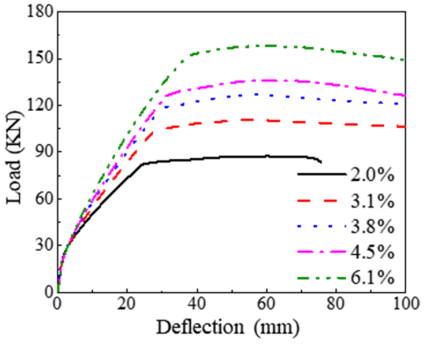


Figure 14. Analysis results of composite slabs with different reinforcement ratios.

3.3.2. Analysis of Specimen Damage Mechanism

The tensile damage contours of the UHPC slab and the stress contours of the steel plate and pegs in the finite element model for specimens N-SUCS-3.1%-150 and N-SUCS-3.1%-250 at ultimate load are depicted in Figures 15 and 16, respectively. It is evident that, for specimen N-SUCS-3.1%-150, none of the pegs in the shear span section yield during ultimate load due to the high degree of shear connection, allowing the steel plate and UHPC slab to achieve cooperative deformation. Furthermore, at ultimate load, the UHPC slab experiences full-section tension, while the steel plate at mid-span experiences compression on the lower surface and tension on the upper surface, with the neutral axis of the cross-section lying within the steel plate's thickness. In contrast, for the comparative specimen N-SUCS-3.1%-250, since the degree of shear connection is 100%, all pegs in the shear span section have significantly yielded at ultimate load. The increased interface slip after the pegs have yielded reduces the synergistic performance of the steel plate and UHPC slab, resulting in some of the lower edges of the UHPC slab near the loading point, on the side close to the pure bending section, being in a compressed state. Simultaneously, none of the stresses at the lower edges of the steel plate reach the yield state, indicating that the full strength of the steel plate is not utilized.

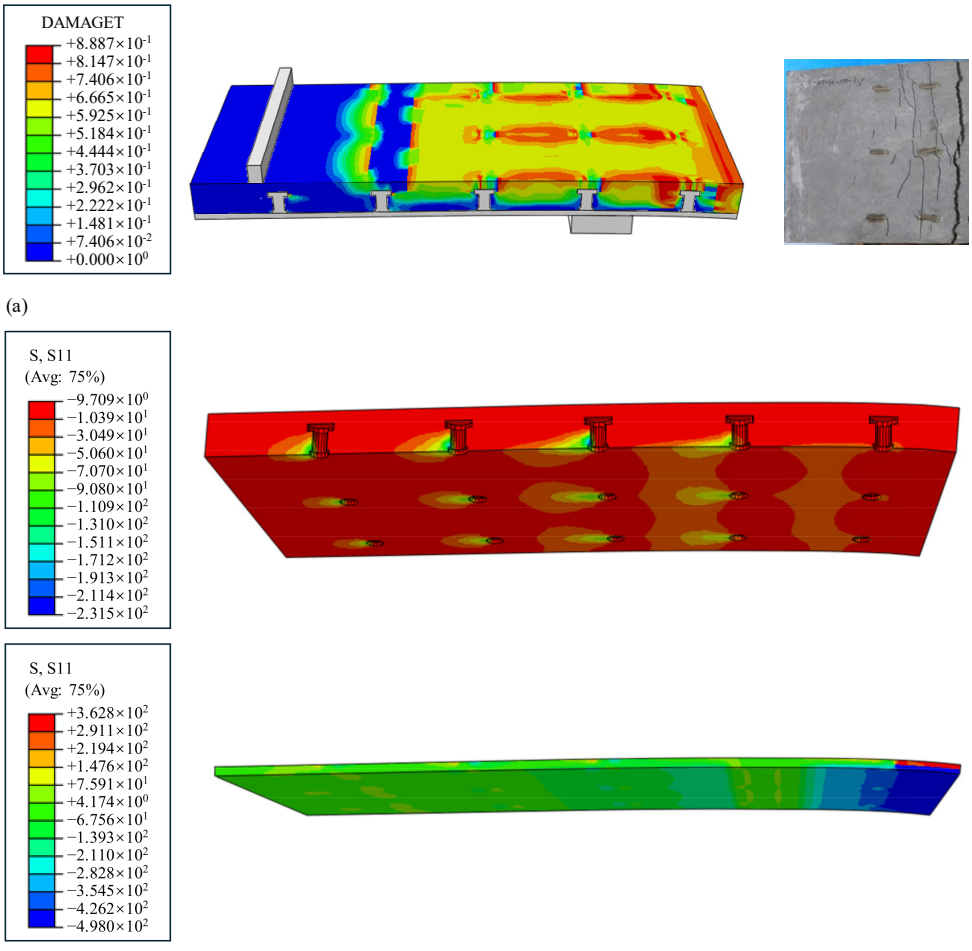
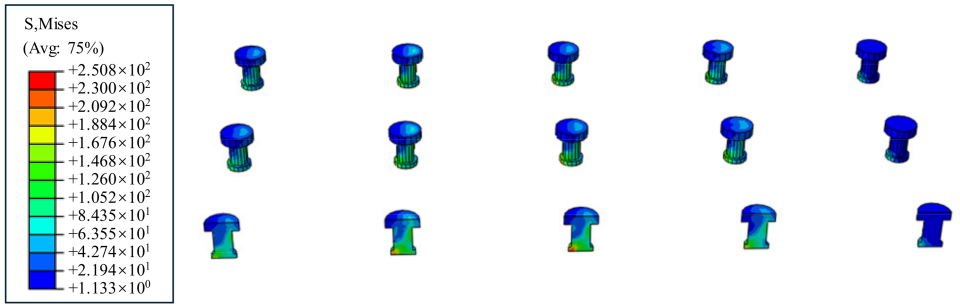


Figure 15. *Cont.*



(c)

Figure 15. Specimen N-SUCS-3.1%-150: (**a**) Tensile damage contours of UHPC slab; (**b**) longitudinal stress contours of UHPC slab and steel plate; (**c**) stress contours of the pegs.

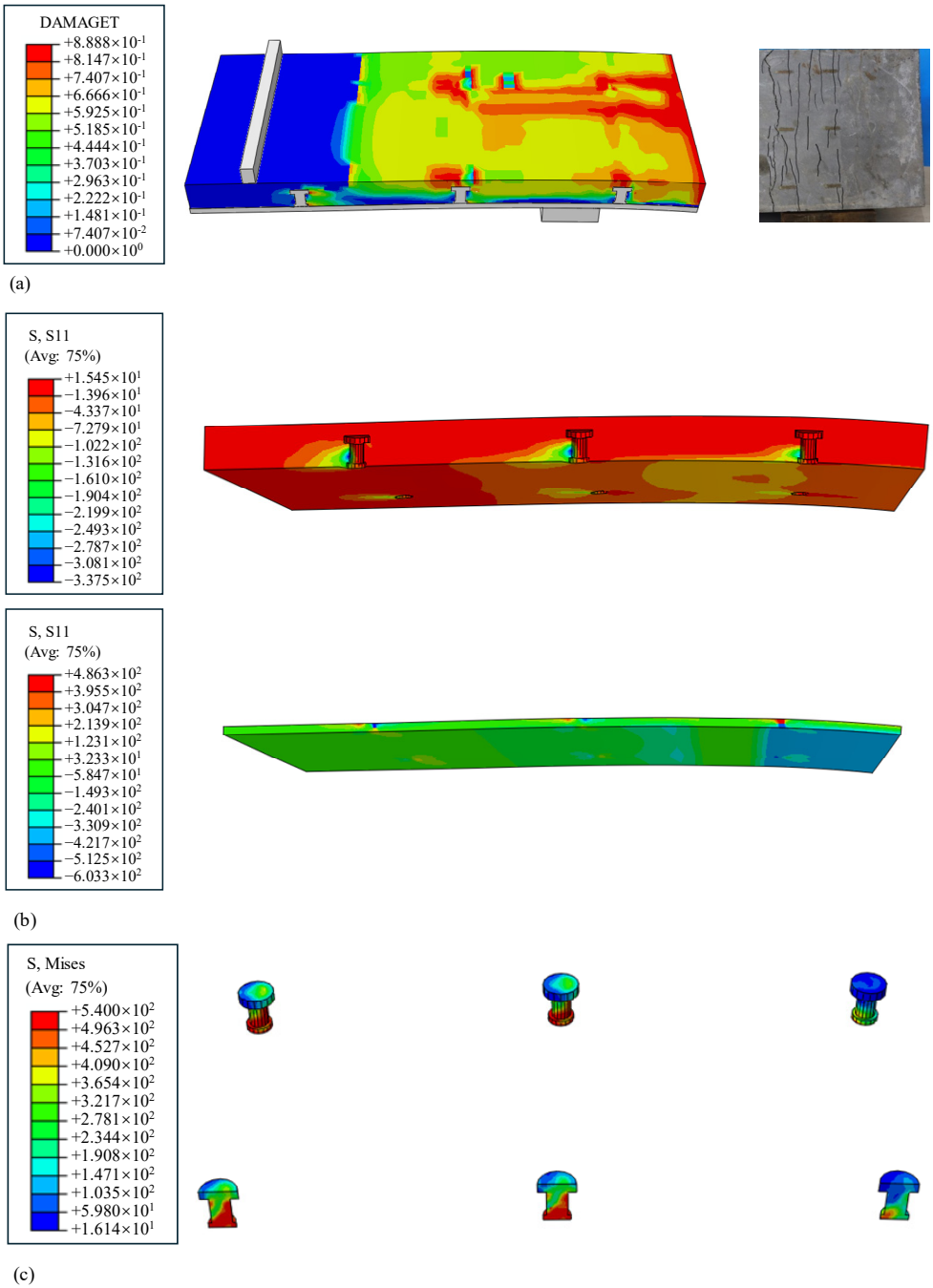


Figure 16. Specimen N-SUCS-3.1%-250: (**a**) Tensile damage contours of UHPC slab; (**b**) longitudinal stress contours of UHPC slab and steel plate; (**c**) stress contours of the pegs.

4. Calculation Method for Load-Bearing Capacity

4.1. Calculation Method for Flexural Capacity Under Positive Bending Moment

According to the results of the test and the numerical simulation, under the action of positive bending moment, when a fully shear-connected composite slab is subjected to ultimate load, the upper surface of the UHPC reaches its ultimate compressive stress and fails in compression, while other locations in the compression zone do not reach their ultimate compressive strength. The entire cross-section of the plate is in tension near the lower surface and yields. When the incompletely connected composite slab is under ultimate load, the UHPC slab undergoes compressive failure. The stress in the steel plate is dependent on the degree of shear connection in the composite slab. When the degree of shear connection is low, during the application of ultimate load, significant interface slip arises. Consequently, both the steel plate and the UHPC slab display a plastic neutral axis within the height of their cross-sections. To facilitate formula derivation and simplify calculations, given that the thickness of the steel plate in steel–UHPC composite structures is generally thinner compared to the thickness of the UHPC, the following assumptions are made in order to calculate the bearing capacity of steel–UHPC composite slabs under positive bending moments: (1) the tensile zone of the steel plate reaches the yield strength, ignoring the role of the compressive zone of the steel plate; (2) the distribution of the stress in the compressive zone of the UHPC is an inverted triangle, and the maximum compressive stress is the compressive strength of the UHPC, corresponding to the cross-section of the UHPC. The maximum compressive stress is the compressive strength of UHPC, and the corresponding cross-section stress distribution model is shown in Figure 17.

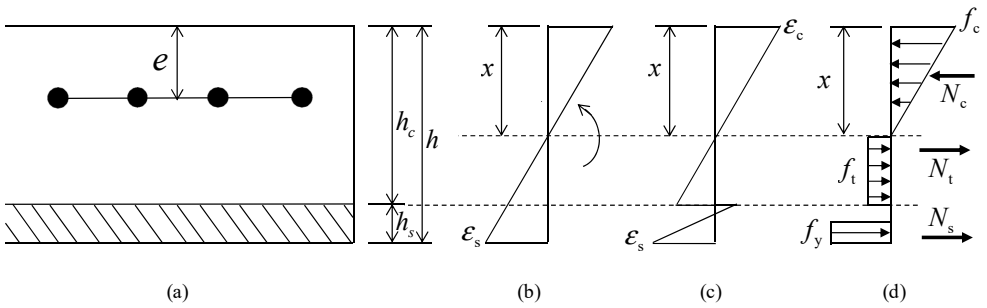


Figure 17. Calculation model of ultimate load under positive bending moment: (**a**) Composite plate cross-section calculation sketch; (**b**) Cross-sectional Strain Distribution-Full Shear Connection; (**c**) Cross-sectional strain distribution-Incomplete shear connection; (**d**) Cross-sectional stress distribution.

According to Figure 17d, the following equation can be obtained based on the axial force balance of the UHPC layer cross-section:

$$N_c - N_t - F_d = 0 \tag{10}$$

$$0.5 f_c b x - f_t b (h_c - x) - F_d = 0 \tag{11}$$

where f_c refers to the compressive strength of UHPC and f_t refers to the tensile strength of UHPC. The positive moment calculation takes the elastic tensile strength of UHPC, which, according to the results of the axial tensile test, is 7.42 Mpa; b refers to the width of the composite slab; x refers to the height of the neutralization axis; h_c refers to the thickness of the UHPC slab; h_s refers to the thickness of the steel plate; N_c, N_t, and N_s refer to the axial forces in the compressive region of the UHPC, the tensile region of the UHPC, and the tensile region of the steel plate; F_d refers to the shear-bearing capacity of the peg connections in the shear span section; and $F_d \leq \min(f_c b h_c, f_y b h_s)$.

From the axial force balance of the steel plate, we obtain the following calculation:

$$N_s = F_d = f_y b x_b \tag{12}$$

where x_b is the height of the tensile zone of the steel plate.

The equilibrium equation for the bending moment of the cross-section is as follows:

$$M = \frac{1}{3} f_c b x^2 + \frac{1}{2} f_t b (h_c - x)^2 + F_d (h - x) - \frac{1}{2 f_y b} {F_d}^2 \tag{13}$$

According to the boundary conditions of the four-point bending steel–UHPC composite slab, the relationship between the bending moment of the pure bending section cross-section and the vertical load can be expressed as follows:

$$p = \frac{2M}{a_0} \tag{14}$$

where a_0 is the length of the shear span section of the composite slab specimen, 500 mm.

Table 7 lists the comparisons of the ultimate bearing capacity of each steel–UHPC composite slab under a positive bending moment calculated according to Equations (10)–(14) based on the results of tests and finite element calculations, and it can be seen that the calculation results of the proposed formula can match the test results better, which can be used as a reference for designers.

Table 7. Theoretical calculation results of flexural bearing capacity under positive bending moments.

Specimen Number	$P_{u,Test}$ (kN)	$P_{u,FEA}$ (kN)	$P_{u,Cal}$ (kN)	$P_{u,Test}/P_{u,Cal}$	$P_{u,FEA}/P_{u,Cal}$
P-SUCS-3.1%-150	320.2	-	314.5	1.02	-
P-SUCS-3.1%-200	285.7	-	272.6	1.05	-
P-SUCS-3.1%-250	159.1	-	166.4	0.96	-
P-SUCS-3.1%-150-FEA1	-	340.5	334.6	-	1.02
P-SUCS-3.1%-150-FEA2	-	343.5	334.6	-	1.03

Note: $P_{u,Cal}$ refers to the calculated ultimate load.

4.2. Calculation Method of Flexural Capacity Under Negative Bending Moment

4.2.1. Theoretical Calculation of Cracking Load of Steel–UHPC Composite Slab

Under negative bending moments, the UHPC layers in steel–UHPC composite slabs are in a state of tension, posing a risk of cracking that could degrade structural durability. To ensure compliance with durability requirements and serviceability limit states specified in relevant codes, during structural design, it is essential to keep the maximum tensile stress in the UHPC layer within its design cracking strength, also referred to as the elastic ultimate strength, in the negative moment region [56]. In UHPC structures, the cracking load is generally defined as the load that corresponds to a maximum crack width of 0.05 mm in the UHPC layer. The UHPC used in this study is all strain-strengthening UHPC. Therefore, when the maximum crack width on the surface of the UHPC slab reaches 0.05 mm under negative bending moments, the corresponding surface strain of the UHPC exceeds its elastic ultimate tensile strain. When the UHPC slab reaches its cracking load, the neutral axis of the composite slab's cross-section is located within the UHPC slab, and the stress and strain distributions across the composite slab section are depicted in Figure 18.

The cracking strain of UHPC is assumed to be ε_{tc}, and according to the flat section assumption, the strain in the steel reinforcement is shown in Equation (15). The elastic ultimate tensile strain of UHPC (ε_{te}) is shown in Equation (16). The strains on the upper (ε_{tsc}) and lower surfaces of the steel plate (ε_{bsc}) are shown in Equations (17) and (18).

$$\varepsilon_{st} = \frac{\varepsilon_{tc}(x-e)}{x} \tag{15}$$

$$\varepsilon_{te} = \frac{\varepsilon_c x_1}{x} \tag{16}$$

$$\varepsilon_{tsc} = \frac{\varepsilon_c(h_c-x)}{x} \tag{17}$$

$$\varepsilon_{bsc} = \frac{\varepsilon_c(h-x)}{x} \tag{18}$$

where x refers to the height of the tensile zone of the UHPC slab, e refers to the thickness of the protective layer of the steel reinforcement, and x_1 refers to the height of the UHPC slab where the strain remains below the elastic ultimate tensile strain of UHPC.

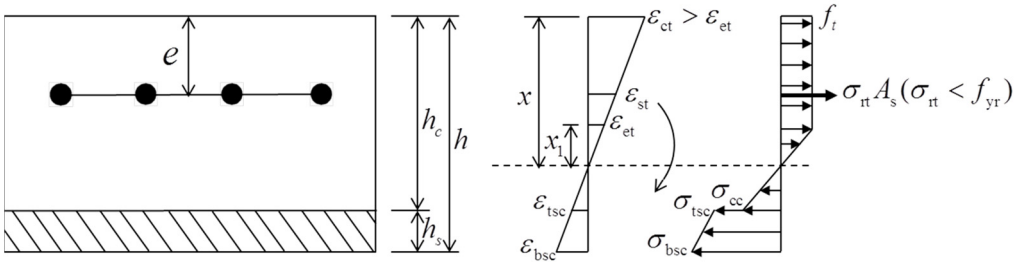


Figure 18. Calculation model of cracking load under negative moment action.

The axial force equilibrium condition of the cross-section is shown in Equation (19). The axial forces borne by the UHPC slab, steel reinforcement, and steel plate are shown in Equations (20)–(22).

$$N_c + N_r + N_s = 0 \tag{19}$$

$$N_c = f_{tu}b(x-x_1) + 0.5f_{tu}x_1b - 0.5E_c\varepsilon_{tsc}b(h_c-x) \tag{20}$$

$$N_r = E_{rs}\varepsilon_{st}A_s \tag{21}$$

$$N_s = 0.5E_sh_sb(\varepsilon_{tsc} + \varepsilon_{bsc}) \tag{22}$$

where N_c, N_r and N_s refer to the axial forces borne by the UHPC, steel reinforcement, and steel beams, respectively. E_{rs} and E_s refer to the modulus of elasticity of the steel reinforcement and steel plate, respectively, and A_s refers to the cross-sectional area of the steel reinforcement.

According to the cross-section moment equilibrium condition, the cracking moment of the steel–UHPC composite slab is shown in Equation (23). The bending moments borne by the UHPC slab, steel reinforcement, and steel plate are shown in Equations (24)–(26).

$$M_{cr} = M_c + M_r + M_s \tag{23}$$

$$M_c = 0.5f_{tu}b(x^2-x_1^2) + \frac{1}{3}f_{tu}bx_1^2 + \frac{1}{3}E_cb\varepsilon_{tsc}(h_c-x)^2 \tag{24}$$

$$M_r = E_{rs}\varepsilon_{st}A_s(x-e) \tag{25}$$

$$M_s = E_sh_sb[(\frac{1}{3}h_s + \frac{1}{2}h_c - \frac{1}{2}x)\varepsilon_{tsc} + (\frac{1}{6}h_s + \frac{1}{2}h_c - \frac{1}{2}x)\varepsilon_{bsc}] \tag{26}$$

where M_c, M_r, and M_s refer to the bending moments borne by the UHPC, steel reinforcement and steel beams, respectively, and M_{cr} refers to the section cracking moment caused by external loads. The above derivation process demonstrates that if the cracking strain ε_{tc} is known, the height x of the tensile zone of the UHPC can be determined using Equation (19). Subsequently, the cracking moment of the steel–UHPC composite slab can be calculated by applying Equation (23).

To determine the cracking strain ε_{tc} of UHPC in steel–UHPC composite slabs subjected to negative bending moments, the cracking loads of the composite slabs are calculated using the aforementioned formula across a range of cracking strains from 0.08% to 0.15%. The outcomes of these calculations are illustrated in Figure 19. By comparing the load values recorded during testing when cracks reached 0.05 mm with the cracking loads corresponding to various cracking strains depicted in Figure 19, the cracking strains of UHPC in each specimen were determined. Table 8 lists the cracking strains ε_{tc} of UHPC in the composite slab specimens, as determined by this method. It can be observed that, under negative bending moments, the cracking strain of UHPC in steel–UHPC composite slabs falls within a range of 0.099% to 0.139%, which is less than the ultimate tensile strain of UHPC measured in axial tensile tests. This is likely due to the uneven distribution of steel fibers resulting from the influence of pegs and steel reinforcement during the pouring of UHPC, subsequently leading to a reduction in the mechanical properties of UHPC.

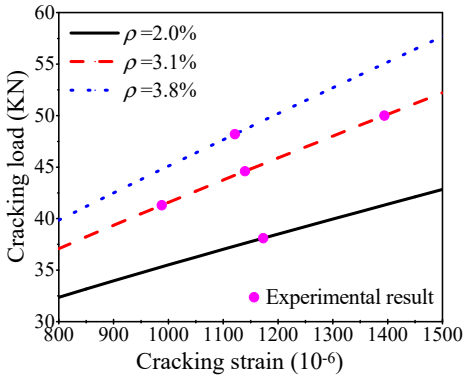


Figure 19. Corresponding relationship between cracking strain and cracking load.

Table 8. Theoretical calculation results of cracking strain of steel–UHPC composite slab.

Specimen Number	$P_{cr,Test}$ (kN)	ε_{tc} (%)	ε_{bst} (%)	ε_{bsc} (%)	$\varepsilon_{bst}/\varepsilon_{bsc}$
N-SUCS-3.1%-150	50	0.139	0.0273	0.0271	1.01
N-SUCS-3.1%-200	44.6	0.114	0.0251	0.0254	0.99
N-SUCS-3.1%-250	41.3	0.099	0.0230	0.0236	0.97
N-SUCS-2.0%-200	38.1	0.117	0.0222	0.0220	1.01
N-SUCS-3.8%-200	48.2	0.112	0.0290	0.0285	1.02

Note: $P_{cr,Test}$ refers to the cracking load obtained from the test, ε_{bst} refers to the experimental lower surface strain of the steel plate, and ε_{bsc} refers to the calculated lower surface strain of the steel plate.

To verify the accuracy of the formula presented in this paper for calculating the cracking strain of UHPC, the strain on the lower surface of the steel plate under the cracking load, calculated using Equation (18), is compared with the measured strain of the steel plate. The comparison results, listed in Table 8, indicate that the calculated results are relatively close to the test results, with the error kept within 3%.

4.2.2. Theoretical Calculation of Ultimate Load of Steel–UHPC Composite Slab

According to the results of the test and finite element analysis, under the action of a negative moment in an incompletely connected composite slab, the degree of constraint that the steel plate exerts on the bending deformation of the UHPC decreases, leading to premature cracking of the UHPC and a reduction in the stiffness and durability of the composite slab. Considering that achieving complete connection of the composite slab under negative moments is relatively feasible in practical engineering, this paper only derives the ultimate load capacity of the composite slab under negative moments and complete connection. For specimens with complete shear connection, at the ultimate load,

the neutral axis of the section is located within the thickness of the steel plate. The lower surface of the steel plate yields under compression, while the UHPC experiences tension across the entire section. With reference to the Swiss specification MCS-EPFL [57], the height of the tensile zone of the reinforced UHPC slab is set at 0.9 h_c. Combining the results of the test and finite element analysis, the ultimate load-carrying capacity of the composite slab is calculated using the method applicable to steel–UHPC composite slabs under negative moments. The following basic assumptions are applied when calculating the ultimate load-carrying capacity: (1) the tensile and compressive zones of the steel plate have reached the yield strength; (2) neglecting the slip between the steel plate and the reinforced UHPC slab, the composite slab conforms to the flat cross-section assumption, and the corresponding cross-section stress distribution model is shown in Figure 20.

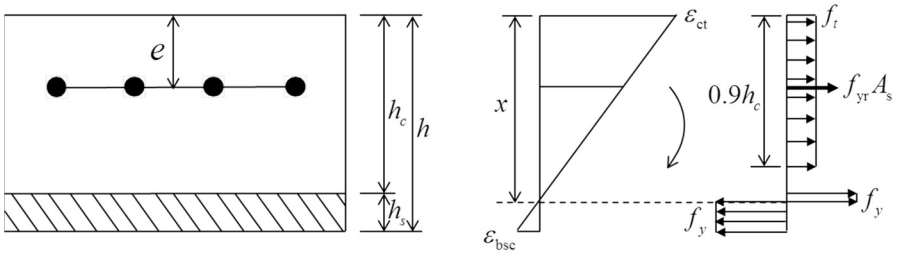


Figure 20. Calculation model of ultimate load under negative bending moments.

The axial force and bending moment equilibrium conditions are shown in Equations (27) and (28).

$$0.9f_t bh_c + f_{yr}A_s + f_y b(x - h_c) = f_y b(h - x) \quad (27)$$

$$M = 0.9f_t bh_c(x - 0.45h_c) + f_{yr}A_s(x - e) + 0.5f_y b[(x - h_c)^2 + (x - h)^2] \quad (28)$$

where A_s refers to the cross-sectional area of the steel reinforcement and f_{yr} refers to the tensile strength of the reinforcement. According to Equation (14), the ultimate bending moment corresponding to the ultimate load can be further calculated for each specimen and cross-section. The calculation results are presented in Table 9. It can be observed that the formula proposed in this paper, which calculates the ultimate load-bearing capacity of steel–UHPC composite slabs under negative bending moments, aligns well with the test results.

Table 9. Theoretical calculation results of bending capacity under negative bending moments.

Specimen Number	$P_{u,Test}$ (kN)	$P_{u,Cal}$ (kN)	$P_{u,Test}/P_{u,Cal}$
N-SUCS-3.1%-150	116.3	112.4	1.03
N-SUCS-3.1%-200	112.6	112.4	1.00
N-SUCS-3.1%-250	110.5	112.4	0.98
N-SUCS-2.0%-200	86.8	90.85	0.96
N-SUCS-3.8%-200	128.2	125.3	1.02

5. Conclusions

A detailed numerical model of steel–UHPC composite slabs is established using ABAQUS software to conduct finite element analyses under positive and negative bending moments. The results are compared with experimental data to validate the accuracy of the finite element model. Based on the finite element analysis results, the stress and damage distribution of each component of the composite slabs under different loading conditions is analyzed. Finally, based on the experimental and finite element analyses, a calculation method for the load-bearing capacity of steel–UHPC composite slabs under positive and negative bending moments is proposed. The main conclusions are as follows:

(1) The load–deflection curves and failure modes obtained from the finite element analysis of the composite slabs show good agreement with the experimental results, indicating that the finite element model established in this study accurately reflects the mechanical behavior of the composite slabs under positive and negative bending moments.
(2) Under positive bending moment conditions, a shear connection degree of 100% in the pegs serves as the critical threshold that changes the mechanical behavior of the specimen. When the shear connection degree exceeds 100%, further increases do not lead to significant changes in the load-bearing capacity of the specimen, although a slight improvement in stiffness can be observed. Conversely, when the shear connection degree is less than 100%, the ultimate load-bearing capacity of the composite slab is governed by the shear capacity of the peg connections. At the ultimate load, significant plastic deformation occurs in the pegs within the shear span, and both the stiffness and load-bearing capacity of the composite slab decrease as the shear connection degree reduces.
(3) Under negative bending moment conditions, when the UHPC and steel plate are in full shear connection, further increasing the shear connection degree for composite slabs with the same reinforcement ratio results in a noticeable improvement in stiffness. Additionally, the crack development on the surface of the UHPC is effectively suppressed. However, the load-bearing capacity remains unchanged, as it is governed by the tensile strength of the UHPC and the reinforcement. For composite slab specimens with the same shear connection degree, increasing the reinforcement ratio of the UHPC effectively enhances both the load-bearing capacity and stiffness of the composite slab. This indicates that increasing the reinforcement ratio significantly improves the crack control capacity of the UHPC.
(4) Based on the experimental and finite element analysis results, the calculation formulas for the load-bearing capacity of steel–UHPC composite slabs under positive and negative bending moments are proposed. The difference between the calculated results and experimental results is less than 3%, which demonstrates the high accuracy of the calculation formulas proposed in this study.

Author Contributions: Conceptualization, X.G.; methodology, C.L.; software, X.G.; validation, B.Z. and X.Z.; formal analysis, C.L.; investigation, D.H., H.B. and X.Z.; resources, H.B.; data curation, B.Z. and X.Z.; writing—original draft preparation, X.G.; writing—review and editing, C.L.; visualization, D.H.; supervision, X.G.; project administration, X.G.; funding acquisition, X.G. All authors have read and agreed to the published version of the manuscript.

Funding: This work was supported by the National Natural Science Foundation of China [Grant No. 52208242], Key Research and Development Special Project of Henan Province (241111322600), the China Postdoctoral Science Foundation [Grant No. 2023M733356], Scientific and technological research and development projects of China Construction Seventh Engineering Division Corp Ltd. (047H2023TM047).

Institutional Review Board Statement: Not applicable.

Informed Consent Statement: Not applicable.

Data Availability Statement: All data generated or analyzed during this study are included in this article.

Conflicts of Interest: We declare that we have no financial and personal relationships with other people or organizations that can inappropriately influence our work. There is no professional or other personal interest of any nature or kind in any product, service, and/or company that could be construed as influencing the position presented in, or the review of, the manuscript entitled "A Numerical and Theoretical Investigation of the Flexural Behavior of Steel–Ultra-High-Performance Concrete composite slabs".

References

1. Amran, M.; Huang, S.S.; Onaizi, A.M.; Makul, N.; Abdelgader, H.S.; Ozbakkaloglu, T. Recent trends in ultra-high performance concrete (UHPC): Current status, challenges, and future prospects. *Constr. Build. Mater.* **2022**, *352*, 129029. [CrossRef]
2. Pan, B.Z.; Liu, F.; Zhuge, Y.; Zeng, J.J.; Liao, J.J. ECCs/UHPFRCCs with and without FRP reinforcement for structural strengthening/repairing: A state-of-the-art review. *Constr. Build. Mater.* **2022**, *316*, 125824. [CrossRef]
3. Zhang, Y.; Zhu, Y.P.; Qu, S.Q.; Kumar, A.; Shao, X.D. Improvement of flexural and tensile strength of layered-casting UHPC with aligned steel fibers. *Constr. Build. Mater.* **2020**, *251*, 118893. [CrossRef]
4. Bajaber, M.A.; Hakeem, I.Y. UHPC evolution, development, and utilization in construction: A review. *J. Mater. Res. Technol.* **2021**, *10*, 1058–1074. [CrossRef]
5. Shafieifar, M.; Farzad, M.; Azizinamini, A. Experimental and numerical study on mechanical properties of Ultra High Performance Concrete (UHPC). *Constr. Build. Mater.* **2017**, *156*, 402–411. [CrossRef]
6. Li, J.Q.; Wu, Z.M.; Shi, C.J.; Yuan, Q.; Zhang, Z.H. Durability of ultra-high performance concrete—A review. *Constr. Build. Mater.* **2020**, *255*, 119296. [CrossRef]
7. Dong, L.; Yang, Y.K.; Liu, Z.X.; Yang, T.; Xue, C.H.; Shao, R.Z.; Wu, C.Q. Effect of chloride ion migration behaviour on the microstructure and mechanical properties of ultra-high performance concrete: A review. *J. Build. Eng.* **2024**, *82*, 108233. [CrossRef]
8. Mousavinejad, S.H.G.; Sammak, M. Strength and chloride ion penetration resistance of ultra-high-performance fiber reinforced geopolymer concrete. *Structures* **2021**, *32*, 1420–1427. [CrossRef]
9. Zhongya, Z.; Kun, P.; Lihao, X.; Yang, Z.; Jun, Y.; Chuanbiao, W. The bond properties between UHPC and stone under different interface treatment methods. *Constr. Build. Mater.* **2023**, *365*, 130092. [CrossRef]
10. Li, Y.; Zhou, H.; Zhang, Z.; Yang, J.; Wang, X.; Wang, X.; Zou, Y. Macro-micro investigation on the coefficient of friction on the interface between steel and cast-in-place UHPC. *Eng. Struct.* **2024**, *318*, 118769. [CrossRef]
11. Gao, X.L.; Wu, K.; Guo, Y.Q.; Zhao, Y.C.; Guo, J.Y. Experimental and numerical study on flexural behaviors of damaged RC beams strengthened with UHPC layer using the bonding technology of post-installed reinforcing bar. *Constr. Build. Mater.* **2023**, *391*, 131835. [CrossRef]
12. Chen, C.; Cai, H.Y.; Cheng, L.J. Shear Strengthening of Corroded RC Beams Using UHPC-FRP Composites. *J. Bridge Eng.* **2021**, *26*, 04020111. [CrossRef]
13. Zeng, J.J.; Liang, Q.J.; Cai, W.J.; Liao, J.J.; Zhou, J.K.; Zhu, J.Y.; Zhang, L.H. Strengthening RC square columns with UHP-ECC section curvilinearization and FRP confinement: Concept and axial compression tests. *Eng. Struct.* **2023**, *280*, 115666. [CrossRef]
14. Sun, L.P.; Liu, Y.J.; Han, Q.; Wang, L. Conceptual design of lightweight assembled double-skinned UHPC composite pylons for large-span suspension bridges. *Structures* **2024**, *70*, 107725. [CrossRef]
15. Leng, J.C.; Yang, J.; Zhang, Z.Y.; Zou, Y.; Du, J.; Zhou, J.T. Mechanical behavior of a novel compact steel-UHPC joint for hybrid girder bridges: Experimental and numerical investigation. *J. Constr. Steel Res.* **2024**, *218*, 108742. [CrossRef]
16. Xiao, J.L.; Yang, T.Y.; Nie, X.; Li, B.Y.; Fan, J.S.; Shu, B.A. Experimental and numerical investigation on mechanical performance of continuous steel-UHPC composite slabs. *Eng. Struct.* **2022**, *270*, 114804. [CrossRef]
17. Gao, X.L.; Wang, M.L.; Guo, J.Y.; Li, H.X. Flexural behaviors of a novel precast hollow UHPC composite beam reinforced with inverted T-shaped steel: Experimental investigation and theoretical analysis. *J. Build. Eng.* **2024**, *86*, 108893. [CrossRef]
18. Gao, X.L.; Yin, C.L.; Guo, J.Y.; Chen, G.X.; Huang, H.R. Experimental and theoretical study on the shear behaviors of an innovative precast UHPC composite beams reinforced with inverted T-shaped steel. *J. Build. Eng.* **2024**, *96*, 110504. [CrossRef]
19. Tong, J.Z.; Chen, Y.L.; Li, Q.H.; Xu, S.L.; Zeng, T.; Gao, W. Experimental study on flexural performance of steel-UHTCC composite bridge decks considering different shear connection degrees. *Eng. Struct.* **2023**, *281*, 115738. [CrossRef]
20. Shao, X.D.; Cao, J.H.; Yi, D.T.; Chen, B.; Huang, Z.Y. Study on the basic performance of orthotropic anisotropic steel plate-thin layer RPC combination bridge decks. *China Highw. J.* **2012**, *25*, 40–45. (In Chinese) [CrossRef]
21. He, Z.G.; Lin, P.Z. Research on fatigue performance and optimal design of steel-UHPC composite slab. *Structures* **2022**, *43*, 682–695. [CrossRef]
22. Zhang, X.H.; Yang, X.Y.; Li, C.; Xu, F.; Wang, G.D. Friction affected fatigue behavior of steel-UHPC composite structures and the fatigue crack growth in studs. *Int. J. Fatigue* **2023**, *177*, 107949. [CrossRef]
23. Li, C.X.; He, L.F.; Pei, B.D.; Pan, R.S.; Shi, Y. Fatigue behavior and damage mechanism of steel plate-UHPC composite bridge deck subjected to negative bending moment. *Structures* **2024**, *65*, 106754. [CrossRef]
24. Xian, B.X.; Wang, G.D.; Ma, F.Y.; Fang, S.; Jiang, H.B.; Xiao, J.J. Shear performance of single embedded nut bolted shear connectors in precast steel-UHPC composite beams under combined tension-shear loads. *Case Stud. Constr. Mater.* **2024**, *21*, e03558. [CrossRef]
25. Zhang, Y.J.; Zhu, J.H.; Wu, L.L.; Lin, H.X.; Fang, Z.C.; Cen, Z.C.; Yang, Y.M.; Fang, S. Experimental and numerical analyses on the shear behavior of grouped single-embedded-nut high-strength bolts in steel-ultra-high-performance concrete composite slabs. *J. Build. Eng.* **2024**, *86*, 108829. [CrossRef]

26. Zhao, X.L.; Lin, G.; Zhou, Y.W.; Huang, Z.Y. Push-out test behavior and damage detection of steel-UHPC composite using PZT sensing. *Eng. Struct.* **2024**, *305*, 117725. [CrossRef]
27. Jia, J.F.; Ren, Z.D.; Bai, Y.L.; Li, J.; Li, B.; Sun, Y.G.; Zhang, Z.X.; Zhang, J.X. Tensile behavior of UHPC wet joints for precast bridge deck panels. *Eng. Struct.* **2023**, *282*, 115826. [CrossRef]
28. Ren, Z.D.; Jia, J.F.; Li, J.; Hu, M.H.; Li, B.; Han, Q.; Du, X.L. Shear behavior of precast bridge deck panels with UHPC wet joints. *Eng. Struct.* **2024**, *316*, 118569. [CrossRef]
29. Feng, Z.; Li, C.X.; Ke, L.; Yoo, D.Y. Experimental and numerical investigations on flexural performance of ultra-high-performance concrete (UHPC) beams with wet joints. *Structures* **2022**, *45*, 199–213. [CrossRef]
30. Hu, W.X.; Li, C.; Chen, B.C.; Liu, Y.J. Finite element analysis on shear behavior of headed studs in steel-UHPC composite slab. *Structures* **2023**, *52*, 464–475. [CrossRef]
31. Lu, K.W.; Xu, Q.Z.; Wang, M.D.; Yao, Y.M.; Wang, J.Q. Anchorage performance of bolt connection embedded in thin UHPC members. *Structures* **2021**, *34*, 1253–1260. [CrossRef]
32. Zhang, S.; Han, B.; Xie, H.B.; An, M.Z.; Lyu, S. Brittleness of Concrete under Different Curing Conditions. *Materials* **2021**, *14*, 7865. [CrossRef]
33. Luo, J.; Shao, X.D.; Fan, W.; Cao, J.H.; Deng, S.W. Flexural cracking behavior and crack width predictions of composite (steel plus UHPC) lightweight deck system. *Eng. Struct.* **2019**, *194*, 120–137. [CrossRef]
34. Wang, Y.; Cao, J.; Shao, X.; Shen, X. Flexural behavior and crack width prediction of UHPC-steel strip composite decks under sagging moments. *Eng. Struct.* **2023**, *293*, 116581. [CrossRef]
35. Zou, Y.; Zheng, K.D.; Zhou, Z.X.; Zhang, Z.Y.; Guo, J.C.; Jiang, J.L. Experimental study on flexural behavior of hollow steel-UHPC composite bridge deck. *Eng. Struct.* **2023**, *274*, 115087. [CrossRef]
36. Li, P.P.; Shao, X.D.; Cao, J.H.; Liu, Q.W.; Qiu, M.H.; Liu, G. Rational configuration and mechanical properties of the steel-UHPC composite deck system. *J. Constr. Steel Res.* **2024**, *221*, 108880. [CrossRef]
37. Taffese, W.Z.; Zhu, Y.P.; Chen, G.D. Explainable AI based slip prediction of steel-UHPC interface connected by shear studs. *Expert Syst. Appl.* **2025**, *259*, 125293. [CrossRef]
38. Xiao, J.L.; Zhou, M.; Nie, J.G.; Yang, T.Y.; Fan, J.S. Flexural behavior of steel-UHPC composite slabs with perfobond rib shear connectors. *Eng. Struct.* **2021**, *245*, 112912. [CrossRef]
39. Rabi, M. Bond prediction of stainless-steel reinforcement using artificial neural networks. *Proc. Inst. Civ. Eng. Constr. Mater.* **2023**, *177*, 87–97. [CrossRef]
40. Rabi, M.; Abarkan, I.; Shamass, R. Buckling resistance of hot-finished CHS beam-columns using FE modelling and machine learning. *Steel Constr.* **2023**, *17*, 93–103. [CrossRef]
41. Rabi, M.; Shamass, R.; Cashell, K.A. Description of the constitutive behaviour of stainless steel reinforcement. *Case Stud. Constr. Mater.* **2024**, *20*, e03013. [CrossRef]
42. Rabi, M.; Jweihan, Y.S.; Abarkan, I.; Ferreira, F.P.V.; Shamass, R.; Limbachiya, V.; Tsavdaridis, K.D.; Santos, L.F.P. Machine learning-driven web-post buckling resistance prediction for high-strength steel beams with elliptically-based web openings. *Results Eng.* **2024**, *21*, 101749. [CrossRef]
43. Abarkan, I.; Rabi, M.; Ferreira, V.P.F. Machine learning for optimal design of circular hollow section stainless steel stub columns: A comparative analysis with Eurocode 3 predictions. *Eng. Appl. Artif. Intell.* **2024**, *132*, 107952. [CrossRef]
44. Gao, X.L.; Wang, J.Y.; Bian, C.; Xiao, R.C.; Ma, B. Experimental investigation on the behaviour of UHPC-steel composite slabs under hogging moment. *Steel Compos. Struct.* **2022**, *42*, 765–777. [CrossRef]
45. Gao, X.L.; Wang, J.Y.; Yan, J.B. Experimental studies of headed stud shear connectors in UHPC Steel composite slabs. *Struct. Eng. Mech.* **2020**, *74*, 657–670. [CrossRef]
46. Liu, X.; Bradford, M.A.; Chen, Q.-J.; Ban, H. Finite element modelling of steel–concrete composite beams with high-strength friction-grip bolt shear connectors. *Finite Elem. Anal. Des.* **2016**, *108*, 54–65. [CrossRef]
47. Ataei, A.; Bradford, M.A.; Valipour, H.R. Finite element analysis of HSS semi-rigid composite joints with precast concrete slabs and demountable bolted shear connectors. *Finite Elem. Anal. Des.* **2016**, *122*, 16–38. [CrossRef]
48. Luo, Y.B.; Hoki, K.; Hayashi, K.; Nakashima, M. Behavior and Strength of Headed Stud-SFRCC Shear Connection. II: Strength Evaluation. *J. Struct. Eng.* **2016**, *142*, 04015113. [CrossRef]
49. Gao, X.L.; Wang, J.Y.; Guo, J.Y.; Liu, C. Axial tensile mechanical properties and constitutive relation model of ultra-high performance concrete under cyclic loading. *Acta Mater. Compos. Sin.* **2021**, *38*, 3925–3938. [CrossRef]
50. Cao, J.; Shao, X. Finite element analysis of headed studs embedded in thin UHPC. *J. Constr. Steel Res.* **2019**, *161*, 355–368. [CrossRef]
51. Kruszewski, D.; Zaghi, A.E.; Wille, K. Finite element study of headed shear studs embedded in ultra-high performance concrete. *Eng. Struct.* **2019**, *188*, 538–552. [CrossRef]
52. Nguyen, H.T.; Kim, S.E. Finite element modeling of push-out tests for large stud shear connectors. *J. Constr. Steel Res.* **2009**, *65*, 1909–1920. [CrossRef]

53. Kim, S.E.; Nguyen, H.T. Finite element modeling and analysis of a hybrid steel-PSC beam connection. *Eng. Struct.* **2010**, *32*, 2557–2569. [CrossRef]
54. Yan, J.B.; Li, Z.X.; Xie, J. Numerical and parametric studies on steel-elastic concrete composite structures. *J. Constr. Steel Res.* **2017**, *133*, 84–96. [CrossRef]
55. Nie, J.G.; Liu, M.; Ye, L. *Steel-Concrete Combined Structures*; Construction Industry Press: Beijing, China, 2005; pp. 68–72. ISBN 978-711-207-189-0. (In Chinese)
56. Li, W.G.; Shao, X.D.; Fang, H.; Zhang, Z. Experimental study on the bending performance of steel-UHPC composite plate. *Civ. Eng. J.* **2015**, *48*, 93–102. (In Chinese) [CrossRef]
57. MCS-EPFL. *Ultra-High Performance Fibre Reinforced Cement-Based Composites (UHPFRC): Construction Material, Dimensioning and Application*; Swiss Federal Institute of Technology: Zürich, Switzerland, 2016.

Disclaimer/Publisher's Note: The statements, opinions and data contained in all publications are solely those of the individual author(s) and contributor(s) and not of MDPI and/or the editor(s). MDPI and/or the editor(s) disclaim responsibility for any injury to people or property resulting from any ideas, methods, instructions or products referred to in the content.